

# Robotic Inspection and 3D GPR-based Reconstruction for Underground Utilities

Jinglun Feng<sup>1</sup>, Liang Yang<sup>1</sup>, Jiang Biao<sup>2</sup>, Jizhong Xiao<sup>1\*</sup> *Senior Member, IEEE*

**Abstract**—Ground Penetrating Radar (GPR) is an effective non-destructive evaluation (NDE) device for inspecting and surveying subsurface objects (i.e., rebars, utility pipes) in complex environments. However, the current practice for GPR data collection requires a human inspector to move a GPR cart along pre-marked grid lines and record the GPR data in both X and Y directions for post-processing by 3D GPR imaging software. It is a time-consuming and tedious work to survey a large area. Furthermore, identifying the subsurface targets depends on the knowledge of an experienced engineer, who has to make manual and subjective interpretation that limits the GPR applications, especially in large-scale scenarios. In addition, the current GPR imaging technology is not intuitive, and not for normal users to understand, and not friendly to visualize. To address the above challenges, this paper presents a novel robotic system to collect GPR data, interpret GPR data, localize the underground utilities, reconstruct and visualize the underground objects' dense point cloud model in a user-friendly manner. This system is composed of three modules: 1) an vision-aided omni-directional robotic data collection platform, which enables the GPR antenna to scan the target area freely with an arbitrary trajectory, while using a visual-inertial-based positioning module tags the GPR measurements with positioning information; 2) a deep neural network (DNN) migration module to interpret the raw GPR B-scan image into a cross-section of object model; 3) a DNN-based 3D reconstruction method, i.e., GPRNet, to generate underground utility model represented as fine 3D point cloud. Comparative studies on synthetic and field GPR raw data with various incompleteness and noise are performed. Experimental results demonstrate that our proposed method achieves much faster and better performance in GPR data collection and higher resolution in GPR imaging on cross-section estimation and 3D model reconstruction than baseline methods. The GPR-based robotic inspection will provide an effective tool for civil engineers to detect and survey underground utilities.

**Index Terms**—3D reconstruction, back-projection (BP) algorithm, ground penetrating radar (GPR), deep neural network, none-destructive evaluation (NDE).

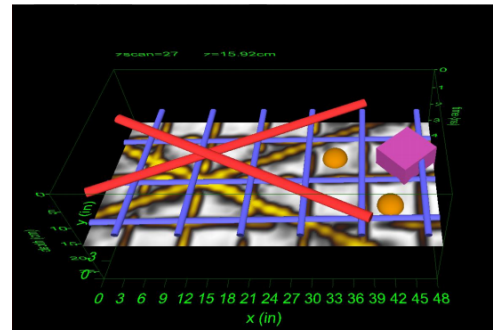
## I. INTRODUCTION

**G**ROUND Penetrating Radar (GPR) is widely used in non-destructive testing (NDT), geophysics survey, and archaeology to locate and map buried objects (e.g., utilities, rebars, underground storage tanks, metallic or plastic conduits), measure pavement thickness and properties, locate and characterize subsurface features (e.g., subgrade voids below concrete slabs or behind retaining walls). The GPR method is a

wave propagation technique that transmits a pulse of polarized high-frequency radar waves into the subsurface media. EM wave attenuates as it travels in media and reflects when it encounters a material change. GPR antenna would thus record the strength and traveled time of each reflected pulse. [1]. The reflections are then amplified, processed, and displayed on a screen as an A-scan signal, analogous to a waveform in an oscilloscope. When the GPR device moves along a straight line, the ensemble of the A-scans forms a B-scan, which is shown as the hyperbolic feature, indicating the objects' locations as well. For 3D investigation, the GPR device scans a target area along grid lines in X-Y perpendicular directions to record the B-Scan data of each scan for post-processing. 3-D GPR imaging software, such as GPR-SLICE [2], implements GPR migration and interpolates the data from multiple scans to produce plan view depth slices, analogous to X-ray images.



(a) Manual survey using Leica DS2000 GPR antenna [3] (b) Manual inspection on the wall with Quantum Mini Concrete Scanner [4]



(c) GPR-SLICE 3D GPR imaging software.

Fig. 1. An illustration of current GPR data collection methods and 3D GPR imaging software: (a) manual survey using a GPR cart, (b) manual inspection on a vertical wall using survey wheel encoder along the grid lines, and (c) 3D GPR imaging software showing the pseudo-3D model reconstructed by traditional GPR migration algorithms.

As illustrated in Fig.1, the current GPR data collection procedure is, first mark/layout a grid covering the inspection area, then push the GPR device along the grid lines and rely on survey wheel encoder to trigger the GPR reading at equal spatial intervals, and it is important to collect and record the

<sup>1</sup>The CCNY Robotics Lab, Electrical Engineering Department, The City College of New York, New York, USA email(jfeng1.lyang1.jxiao@ccny.cuny.edu)

<sup>2</sup>Hostos Community College, New York, NY, USA. email(bjiang@ccny.cuny.edu)

\*Corresponding author.

GPR data in both X and Y directions for post-processing by 3D GPR imaging software. It is a time-consuming and tedious work to surveying a large area. The feedback from the geophysical survey and NDT service providers indicates that it normally takes a two-person team two hours to mark the grid intersection nodes on a 200-feet by 200-feet site. Assuming the grid spacing is 0.5 feet, the total distance to collect GPR data along the grid lines covering the site is 160,000 linear feet (30.3 miles), and the operator must precisely follow the grid lines for the 30.3 miles, a very challenging task, to hopefully get accurate data readings. Other limitations of manual inspection include 1) the inability to obtain position and orientation information from its wheel encoder, 2) the requirement for perpendicular scanning concerning buried pipelines to generate clear B-scan hyperbola images, 3) the requirement to take notes to record these linear motion trajectories for GPR data post-processing, and 4) the inability of the current 3D GPR imaging software to process GPR data collected along non-linear trajectories.

In summary, there are two major pain points for GPR-based NDT and Geophysical Survey: 1) the lack of an effective and efficient tool for automatic GPR data collection in surveying large areas or at critical locations of infrastructure that are difficult to access by human operators; and 2) the lack of effective and efficient 3D GPR data analysis software that can process GPR data collected by scanning the targeted area in arbitrary trajectories.

To address these challenges, we propose a novel sub-surface 3D model reconstruction system for GPR sensors by taking advantage of an Omni-directional robot to collect the raw data, which allows the user to visualize the underground utilities. Inspired by [5], [6], this paper also takes advantage of some DNN-based models to improve the GPR 3D model reconstruction further. The key difference between our methods and existing ones is that only a small amount of GPR data is required for 3D model reconstruction. In the meanwhile, it also generates a better visualization model represented as a point cloud.

The main contributions of this work are:

- an automated GPR data collection solution using an Omni-directional robot, which holds the GPR antenna on the bottom and moves forward, backward, and sideways without any rotations occurred during data collection.
- a DNN model that processes and interprets the GPR B-scan image into a cross-section model of underground objects.
- a novel 3D reconstruction model that takes sparse GPR measurement as input and completes it with a dense point cloud that can present the fine details of the object structure.

## II. RELATED WORKS

Ground Penetrating Radar (GPR) migration and model reconstruction are popular topics in the robotics and civil engineering communities and have been extensively investigated during the past two decades. This paper focuses on a complete solution from data collection to model reconstruction, together with some algorithms exploiting uncertainty.

**Conventional Migration Methods:** The mathematical-based technique which serves as the traditional GPR imaging tools, enabling to convert the unfocused raw B-scan radargram data into a focused target, is called *migration*. Conventional migration methods can be roughly categorized into Kirchhoff migration, the phase-shift migration, the finite-difference method.

Kirchhoff migration method [7] is first introduced in 1970s, [8] tests Kirchhoff migration method by using both synthetic and real GPR data, the results show that though the localization of the buried targets could be achieved, the information about target shape and extension are not provided by implementing this method. In the meanwhile, [9] represents that Kirchhoff migration method is capable to focus on the target position, however, it's processing speed is slower than the rest of migration approaches.

Similar to Kirchhoff migration, phase-shift migration is first proposed and applied in 1978 [10], this is also a mathematical-based method that utilizes the FFT concept [11]. For comparable accuracy, this approach to migration is computationally more efficient than the finite-difference [12] approach, which is designed for the geometry of a single radargram source with a line of surface receivers.

**Back-projection Related Methods:** The back-projection (BP) algorithm is the most significant and common 2D imaging reconstruction method in GPR [1], [13]. When GPR emits the radiation pulse, the conventional BP algorithm assumes this wave path shares a semi-sphere pattern with an equal energy level. After GPR receives the radiation pulse back, the BP algorithm stack the radiation energy along the hyperbolic trajectory, then the sum of the responded amplitude could reflect the target region [14], [15].

To further improve the effectiveness of the convention BP algorithm, several modified BP methods are proposed. X. Xie *et al.* [16] presented the bi-frequency BP (BBP) to enhance the visualization quality of the subsurface objects, especially for grouting. Fast BP (FBP) is proposed by L. Zhou *et al.* [17], it's an approximation method which could run faster by simplifying the computation of subsurface dielectric [18]. In addition, many researches focus on cross-correlation BP (CBP) method [19]–[22] as well, CBP can cut down the round trip time-of-flight from a stimulating source to a focal point and back to a receiver. Moreover, H. Liu *et al.* [23] improved BP algorithm by integrating a correction factor for radiation pattern in the subsurface, to reduce the negative influence of the traditional homogeneous radiation pattern on GPR. Filtered BP (FBP) is another common modified BP method, papers [14], [24] investigated this method to get rid of the noise effects back in the GPR images.

**3D GPR imaging methods:** In recent years, research on 3D GPR imaging has made commendable progress in academia. Prof. Dezhen Song's group at Texas A&M University published a series of papers on automatic subsurface pipeline mapping and 3D reconstruction by fusing a GPR and a Camera [25]–[30]. They model the GPR sensing process and prove hyperbola response for general scanning with non-perpendicular angles, which is novel. They fuse V-SLAM and encoder readings with GPR scans to classify hyperbolas

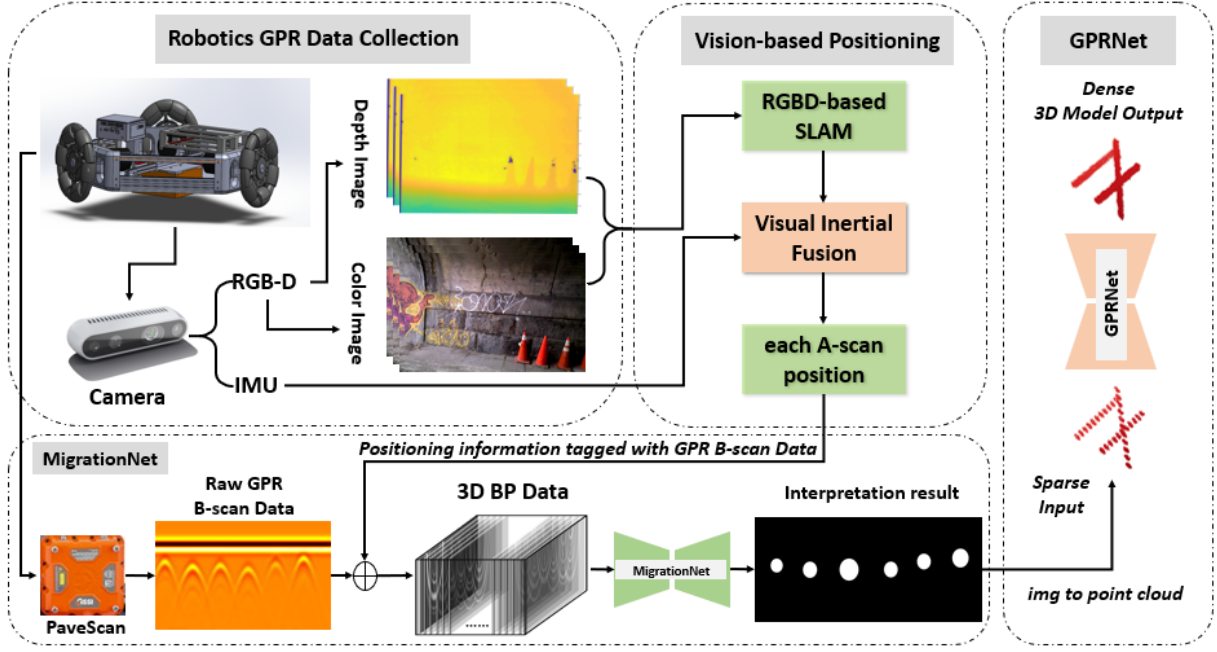


Fig. 2. The omni-directional robot for vision-based GPR data collection, where a GPR antenna is installed at the bottom of the robot chassis.

into different pipeline groups and apply the J-linkage and maximum likelihood method to estimate the radii and locations of all pipelines. However, the average error for pipe radius estimation is over 35%, which is not good enough for practical use [25]. They encounter calibration and synchronization problems and have to use customized artificial landmarks to synchronize camera poses (temporally evenly-spaced) to the GPR data (spatially evenly spaced) [30]. Similarly, M. Pereira *et al.* at the University of Vermont published several papers related to 3D reconstruction from both ground and air-coupled multistatic GPR [31]–[34]. The main contribution of these works is the consideration of phase compensation for different receiver antennas. Not only stack the B-scan images to model the 3D multistatic GPR imaging, but they also take the different obtained gain and dielectric contrast of each receiver antenna into consideration and further fuse it with a Hessian-based enhancement filter to formulate the final 3D reconstruction model. However, the noise reconstructed in the 3D model is still not clearly removed by the proposed method, which makes the 3D model not good enough for visualization. In addition, even if the author proposed another method for integration between GPR scan and positioning information [35], the 3D GPR imaging method they presented could only recover the depth of subsurface objects, which overlooked the x-y direction positioning information.

### III. ROBOTICS GPR INSPECTION SYSTEM OVERVIEW

As illustrated in Fig.2, we propose a novel GPR-based robotic inspection system as a holistic solution to automate the data collection and generate the 3D model of subsurface targets. The robotic inspection system implements visual-inertial Simultaneous Localization and Mapping (SLAM) to estimate the pose and facilitate GPR data collection. We

further analyze the GPR scan through a learning-based module that can interpret the B-scan image to a cross-section image. At last, we propose the GPR pipe reconstruction network (GPRNet) (illustrated in Section.IV) to generate the 3D model of subsurface objects.

#### A. Vision-aided Robotic GPR Data Collection

The current GPR data collection in the industry needs to satisfy multiple requirements. It needs an inspector to calibrate the survey wheel, layout the grid map, take notes and photographs, and manually push the GPR device along the pre-mapped lines. Therefore, to facilitate and automate the GPR data collection/survey, a low latency, low cost, and robust vision-aided robotic data collection solution is implemented in this paper to obtain the 3-DOF pose (X, Y, Theta) of the GPR cart in real-time. We developed an Omni-directional robot for the inspection of underground utilities. Our robot has a triangle-shaped chassis with three specially designed mecanum wheels that allow the robot to move forward, backward, and sideways without rotation. It also carries a GPR antenna to conduct data collection, an RGB-D tracking camera with a 6-axis IMU embedded to provide accurate and robust pose estimation for the GPR sensor, and a high level controller (i.e., Intel NUC) to synchronize the positioning data with GPR scan data.

Specifically, as depicts in Fig.3, our high maneuverable design allows the robot to move in any direction without spinning and thus provide a non-linear arbitrary trajectory for the GPR scanning, the robot motion satisfies the following relation:

$$\begin{bmatrix} v_{w1\_drv} \\ v_{w2\_drv} \\ v_{w3\_drv} \end{bmatrix} = \begin{bmatrix} 1 & 0 & -d \\ \cos \frac{2\pi}{3} & \sin \frac{2\pi}{3} & -d \\ \cos \frac{-2\pi}{3} & \sin \frac{-2\pi}{3} & -d \end{bmatrix} \begin{bmatrix} v_x \\ v_y \\ \omega \end{bmatrix} \quad (1)$$

where  $v_{w1\_drv}$ ,  $v_{w2\_drv}$ ,  $v_{w3\_drv}$  represents the linear velocity of each wheel,  $d$  indicates the distance between the center of a wheel and the center of the robot body.  $v_x$ ,  $v_y$ , and  $\omega$  represent the linear velocity and angular velocity of the robot body respectively.

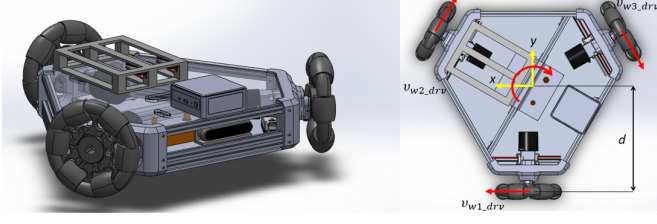


Fig. 3. The Omni-directional robot for vision-based GPR data collection, where a GPR antenna is installed at the bottom of the robot chassis.

We further fuse the IMU and the visual odometry data to improve the positioning accuracy by using a loosely-coupled approach, which was introduced in our previous works [5], [36].

At last, the GPR scan data and pose data are synchronized according to their time stamp, making the GPR data collection significantly easier by enabling the robotic GPR-Cart to scan the surface in arbitrary trajectories.

### B. MigrationNet for GPR Data Interpretation

In this section, we introduce an encoder-decoder learning model, MigrationNet, to interpret B-scan images. Compared with the existing learning-based method of GPR data interpretation [37]–[40], our approach does not focus on detecting hyperbola features in the raw B-scan image, because detection on the GPR B-scan hyperbolic features won't be helpful for GPR data interpretation. MigrationNet takes advantage of the back-projection (BP) algorithm. The BP is a process of aggregation that converts different amplitude of energy into a *semi-sphere* format at different time. As illustrated in Fig.4, the brighter semi-sphere indicates the higher amplitude part in A-scan. Furthermore, the radius of each semi-sphere in the BP image indicates the depth between the ground and the object. Hence, MigrationNet emulates the BP principle, stack each back-projected A-scans into space domain with multi-resolutions, and further interpret them to the cross-section image of the subsurface objects.

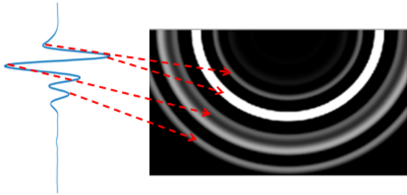


Fig. 4. BP algorithm converts the A-scan raw data into a set of semi-spheres.

1) *Sparse Back Projection Aggregation*: There are some limitations in the conventional BP approach. First of all, it needs to back-project each A-scan into a pre-defined 3D

volumetric map, where each A-scan comes from the same B-scan. Second, as each back-projected A-scan is overlapped into a volumetric map one by one, it leads to heavier computation and processing speed.

To address the above issues, we propose a multi-spatial resolution input, where the resolution denotes how many A-scan measurements from a B-scan are used for back-projection. Specifically, since each B-scan might have a different number of A-scan measurements, for any B-scan data whose number of A-scan measurements are less than 1024, we only pick 256, 128 and 64 A-scan measurements for back-projection and stack them in the spatial domain as the input. This is how we distinguish the different spatial resolution in the input data. Otherwise, for those B-scan data with more than 1024 A-scan signals, we introduce a sliding-window crop operation over the B-scan raw data to split it into several parts. This operation is equivalent to Equ.2. Note that the length of the sliding window is fixed to 1024 while the width is as same as the raw B-scan data, which represents the sampling number of an A-scan measurement.

$$m = \lfloor N/1024 \rfloor \quad (2)$$

where  $N$  is the number of A-scan measurements in a B-scan and  $m$  is the number of cropping B-scans has 1024 A-scans after the trim operation.

In this way, several  $M * N * C$  3D stacked input is created, where  $M$  demonstrates the number of A-scans in the related B-scan,  $N$  indicates the number of the sample data in an A-scan measurement, and  $C$  is the number of BP data in each stack group.

We choose to sparsely aggregate the back-projected data because the proposed MigrationNet can well learn the spatial relationship from the stacked input data as well as interpreting the cross-section image of the subsurface cylindrical model. Moreover, this input data with a sparse resolution can decrease the computational cost and provide richer input information due to the multiple resolutions in the spatial domain. More details will be shown in Section III-B and Section V-B2.

2) *Multiple Spatial Resolution Encoder*: We first introduce our feature extractor, named Multiple Spatial Resolution Encoder (MSRE). It takes advantage of Feature Pyramid Network (FPN) [41], inherits the feature capture ability by introducing a multi-resolution input, and reveals the rich local structure information in the spatial domain. In contrast, the common feature extractor in most related works [42], [43] takes no advantage of the resolution information of the input data. As depicts in Fig.5, the channel numbers of the input BP data indicate the multiple resolution property in the spatial domain.

Specifically, the multiple resolutions of the stacked BP data contain 256 channels, 128 channels, and 64 channels, respectively. Besides, for any B-scan that includes more than 1024 A-scans, we first crop it as introduced in Equ.2. Then, three independent feature extractors will interpret these multiple spatial resolution inputs to the latent feature map  $f$ , following a few down-sampling groups. Each down-sampling group is a combination of two convolution layers and one max-pooling layer. Note that all the encoded feature maps  $f$  share the same size:  $[M \times N \times 512]$ . To implement it, each feature extractor



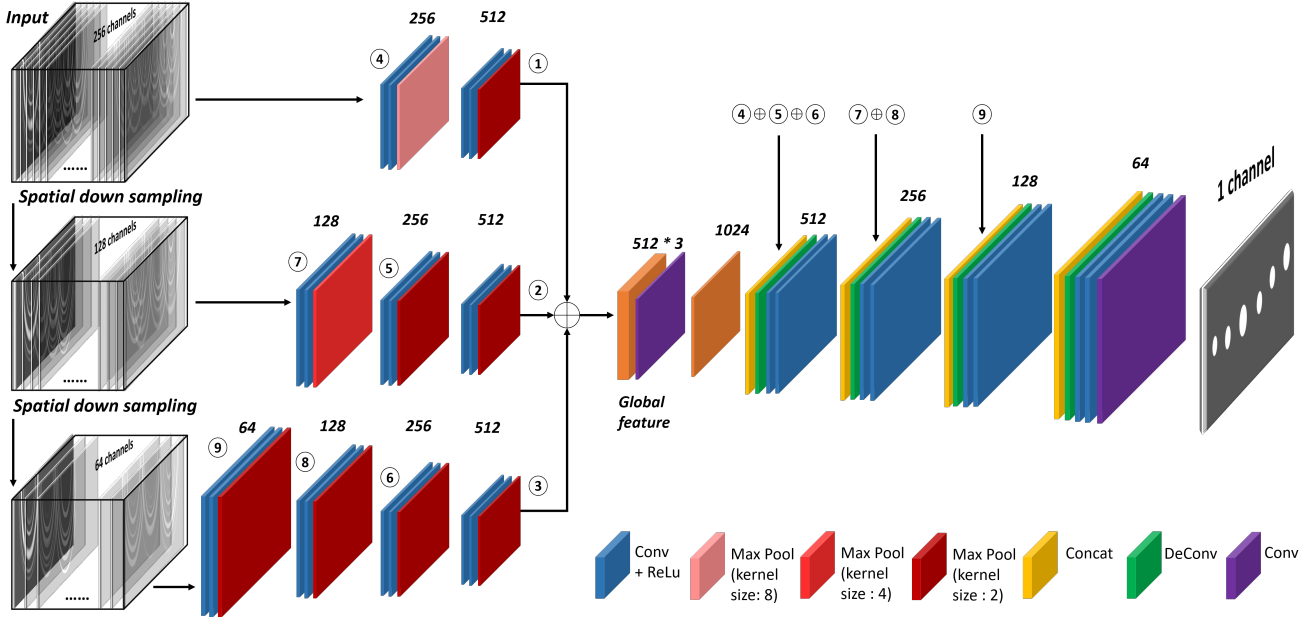


Fig. 5. Schematic of the proposed DNN-based migration framework. The input is the stacked BP data with 256 channels and further down-sampling into 128 and 64 channels in the spatial domain. Then, the global features are extracted through the multiple spatial resolution encoder and further concatenated into 1536 channels. The encoder consists of several de-convolutional groups. The global feature is combined with local features from MSRE through skip-connection operation indicated by  $\oplus$  while ① to ⑨ present the last layer feature in each de-convolutional group, and finally decoded into a binary migration image.

has its unique down-sampling group where the kernel size of the max-pooling layer is different. In detail, the kernel size of the max-pooling layer in the 256 channels input is 8. Meanwhile, for 128 channels input, the kernel size of the first max-pooling layer is 4, while the rest of the pooling layers' kernel size is equal to 2. As 64 channels sparse input, all the kernel sizes of max-pooling layers in the down-sampling groups are 2. As depicts in Fig.5, the different color in the encoder structure indicates the different kernel size of the pooling layer in each down-sampling group.

At last, all three feature maps are then concatenated together as  $F$ , where size =  $[M \times N \times 1536]$ . This design brings the combined latent feature ability to contain better spatial information of the input BP data.

3) *Decoder*: Our decoder consists of 4 up-sampling groups, and each group contains two convolutional layers and one deconvolutional layer. Besides, we also take advantage of skip connections as illustrated in Fig.5. The skip-connection works on the different encoder layers that have the same size. Specifically, layers ④ to ⑥ share the same size, and they are concatenated to the first up-sampling layer. Layer ⑦ and ⑧ are concatenated to the second up-sampling layer for the same reason. At last, layer ⑨ is skip-connected to the third up-sampling layer.

To summarize, the decoder interprets the global feature map  $F$  to a  $[M \times N \times 1]$  migration binary image, where the white region indicates the pipe and the black area indicates the background.

4) *Loss Design and Training*: To constrain the shape and size of the underground cylindrical object, we develop a joint loss in a two-level hierarchy, pixel, and structure-level, which can capture fine structures with clear boundaries. Our hybrid

loss function is composed by following two terms:

Firstly, since most of the non-destructive testing objects have a round shape cross-section (i.e., rebars, utilities, PVC pipes, etc.), we must compare structure similarity between the predicted image and the ground truth to maintain the proper size and shape. Thus, inspired by [44]–[46], we demonstrate the structure comparison loss between predicted image  $X$  and ground truth  $Y$  as follows:

$$L_1 = \frac{\sigma_{xy} + C}{\sigma_x \sigma_y + C} \quad (3)$$

where  $\sigma_x$  and  $\sigma_y$  are the standard deviation as an estimate of the image contrast,  $C$  is a constant value while  $\sigma_{xy}$  represents the covariance which is:

$$\sigma_{xy} = \frac{1}{N-1} \sum_{i=1}^N (x_i - \mu_x)(y_i - \mu_y) \quad (4)$$

where  $\mu_x$  and  $\mu_y$  are mean intensity of the predicted image and ground truth respectively,  $N$  is the number of pixels in the image.

The second loss expression is a common cross entropy loss as proposed in [42]

$$L_2 = \sum_{x_i \in \mathcal{M}} w^j(x) \log(p(x_{i,j})) \quad (5)$$

where  $x_i$  indicates an element in given input while  $M$ ,  $p(x_{i,j})$  is the element  $x_i$  probabilistic prediction over class  $j$ , and  $w^j$  is the weight of each classes.

Finally, our loss function could be illustrated as following:

$$L = \lambda_1 L_1 + \lambda_2 L_2 \quad (6)$$

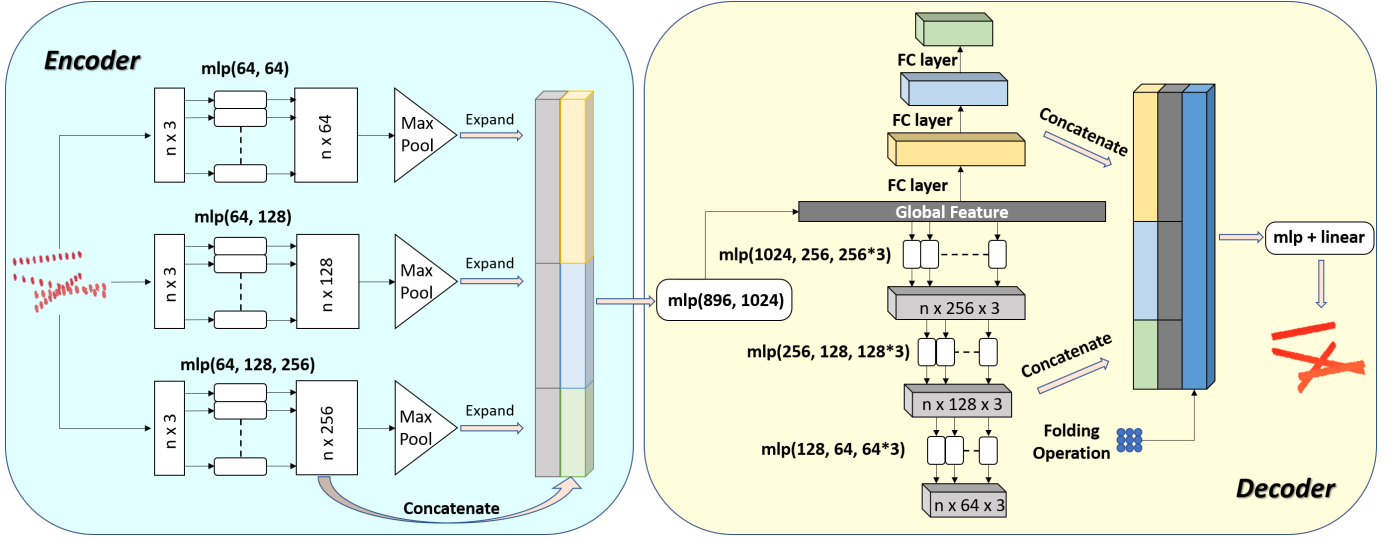


Fig. 6. GPRNet framework. The input is a sparse point cloud representing the cross-section of utilities, the encoder abstracts the input as a global feature, and the decoder recovers the global feature to a dense point cloud.

where  $\lambda_i$  and  $\lambda_j$  are the weight of cross entropy loss and structure loss which satisfy the relation as  $\lambda_i + \lambda_j = 1$ .

**Training:** The weights governing the terms in loss function is set to  $\lambda_i = 0.1$  and  $\lambda_j = 0.9$ , we also use the stochastic gradient descent (SGD), select momentum as 0.9 and weight decay as  $1e-8$ . As for the initial learning rate (LR) and input scale, by evaluating the average accuracy, average precision, average recall as well as F1 score in training dataset with different LR and scale, the learning rate is set to  $5e-6$  while the input scale is 0.25.

#### IV. GPRNET: GPR PIPES RECONSTRUCTION NETWORK FOR 3D MODELLING

MigrationNet facilitates interpreting the raw B-scan image into a cross-section image. However, MigrationNet only provides the 2D slice structure of underground utilities. Even by concatenating the slices into the 3D space, the obtained 3D map is still too sparse to precept. Thus, we manage to complete the gap between this sparse 3D map to recover a dense model of underground utilities.

Inspired by the 3D point cloud completion works [6], [47] in the computer vision area, we propose GPRNet to obtain a dense model of the targets. We firstly represent the interpreted image, which indicates the cross-section of the underground utilities, into the 3D point cloud data format. Our encoder-decoder-based network further completes the sparse input to generate a fine and dense 3D point cloud reconstruction map.

##### A. GPRNET Design

1) *Encoder:* The encoder is an extended version of PCN [6], it represents the geometric information in the input point cloud with a global feature vector  $\mathbf{v} \in \mathbb{R}^n$ ,  $n = 896$ , where this global feature vector is the output of the encoder. Besides, our encoder implements PointNet layer [48] to extract features, while the PointNet layer is a combination of the convolutional multi-layer perceptron (MLP) layer and the max-pooling

layer. This design facilitates our encoder to extract multiple resolution information of the input data, leading to better performance on local structure completion.

Specifically, by passing through three MLP layers with different dimensions, our input  $m \times 3$  point cloud data, where  $m$  is the number of the points set to 1500, is firstly encoded into three point feature vectors  $\mathbf{f}_i$ , where size is equal to  $\mathbf{f}_i := m \times 64$ ,  $m \times 128$ ,  $m \times 256$  for  $i = 1, 2, 3$  respectively. Then, a max-pooling layer is conducted on each extracted feature to obtain three intermediate features  $\mathbf{g}_{j=1,2,3}$  with multiple dimensions  $[64 - 128 - 256]$ . Furthermore, we concatenate each point feature vector  $\mathbf{f}_i$  and each intermediate feature  $\mathbf{g}_j$  together to obtain an expanded feature, which includes the feature information at different level. In addition, each  $\mathbf{g}_j$  is concatenated to each  $\mathbf{f}_i$  to obtain the feature matrix  $\mathbf{F}$ , where the size is  $m \times 896$ . At last,  $\mathbf{F}$  is passed through another PointNet layer to generate the global feature vector  $\mathbf{v}$ .

2) *Decoder:* The fully-connected decoder [49] is good at predicting the global geometry of point cloud. However, it ignores the local features. While FoldingNet decoder [50] is good at generating a smooth local feature. Taking the advantages of both decoders, we introduced a decoder as a hierarchical structure similar to [51].

As shown in Fig.6 decoder part, at the top of the decoder, there are three features (size:=  $256 \times 3, 128 \times 3, 64 \times 3$ ) which are extracted from the global feature by the fully-connected layers. Meanwhile, to get a better structure sense of the input point cloud, the global feature is further down-sampled into the three different levels through the MLP layers. These three down-sampling features share the size:=  $256 \times 3, 128 \times 3, 64 \times 3$  as well. Then, the global and local features are concatenated and represented as an  $896 \times 3$  matrix. At last, by taking advantage of folding operation, a patch of 9 points is generated at each point in the point set generated from the last step. Thus, we can obtain the detailed output consisting of  $896 \times 9$  points. A dense point cloud output is then generated from our multi-resolution decoder, based on the fully-connected and folding

operations.

Thanks to this multi-resolution architecture, high-level features will affect the expression of low-level features. The low-resolution features can contribute to forming the global feature, which provides a sense of the local geometry of the shape. Our experiments show that the prediction of our proposed decoder has fewer distortions and better-detailed geometry of the shape.

3) *Loss Design and Training*: To constrain and compare the difference between the output point cloud  $S$  and the ground truth point cloud  $S_{gt}$ , an ideal loss must be differentiable concerning point locations and invariant to the permutation of the point cloud. In this paper, we use Chamfer Distance (CD) to calculate the average closest point distance between  $S$  and  $S_{gt}$ , that meets the requirement of the above conditions:

$$d_{CD}(S, S_{gt}) = \frac{1}{S} \sum_{x \in S} \min_{y \in S_{gt}} \|x - y\|_2 + \frac{1}{S_{gt}} \sum_{y \in S_{gt}} \min_{x \in S} \|y - x\|_2 \quad (7)$$

The Chamfer Distance finds the nearest neighbor in the ground truth point set. Thus it can force output point clouds to lie close to the ground truth and be piecewise smooth.

**Training**: The training dataset for 3D reconstruction contains 306 models while we reserve 18 models for validation and 36 models for testing. The details of dataset setup will be explained in Section V-A. Notice that our models are trained for 100 epochs with an Adam optimizer. The initial learning rate is set to 0.00005 while the batch size is 16. The weight decay is 0.7 for every 50000 iterations.

## V. EXPERIMENTS STUDY

### A. Data Preparation

To verify the proposed DNN models in this paper, we prepare a GPR B-scan dataset for training and testing purposes. The dataset we provide contains both synthetic and field B-scan data.

1) *Field GPR data Generation*: We firstly collected the field GPR data with our proposed robotics GPR inspection system on a concrete slab at CCNY Robotics Lab Testing Pit. Design of our testing concrete slab with different pipes is defined in Fig. 7, our concrete slab have a dimension of  $96'' \times 36'' \times 8.5''$  (length  $\times$  width  $\times$  thickness), and there are 10 pipes embedded in the slab with different size, depth and material. Specifically, 7 pipes are buried horizontally, 1 copper pipe is set perpendicular to the horizontal pipes, and two pipes are diagonally fixed.

As mentioned in Section III-A, we control the Omnidirectional robot move along zig-zag path to cover the slab, with 11 pipes buried underneath with different sizes and depth. In the end, there are 120 automated GPR tests are conducted, which generate 120 raw B-scan data to contribute to our dataset.

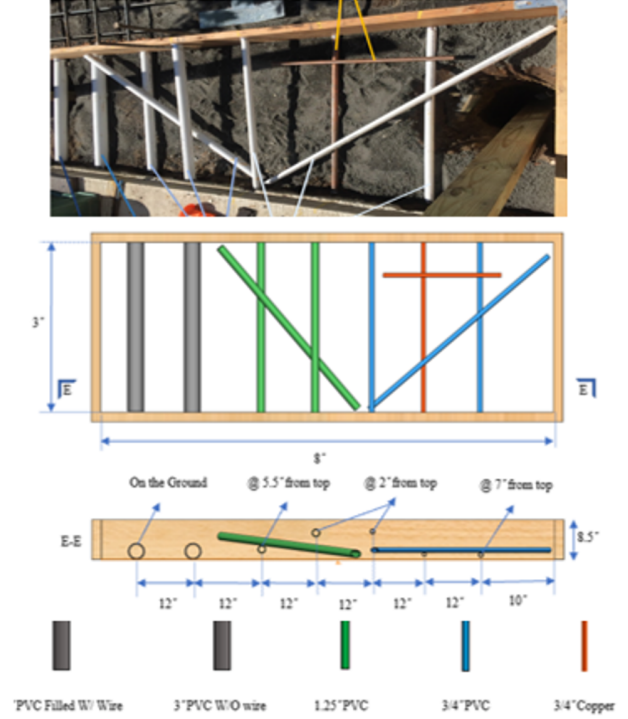


Fig. 7. The design details and ground truth of the concrete slab.

2) *gprMax Data Generation*: However, the collected field data is still not enough for the DNN model training purpose. Thus, by taking advantage of gprMax [52], we build a synthetic testing environment that simulates the real NDT condition.

For those objects that need to be evaluated in a real underground environment, most of them are pipe-shaped with a round cross-section, for example, rebars, utilities, and PVC pipes. Our simulated environment emulates this property and involves pipe-shaped objects with different location as well as the size. Notice that all of the simulated objects have a cylindrical shape. Furthermore, in order to match the data collection in commercial GPR, our synthetic GPR B-scan dataset is finally generated along the line route.

Specifically, we build 567 different synthetic concrete slabs. All the slabs have the same dimension, which is:  $[0.35m (l) \times 0.25m (w) \times 0.25m (d)]$  while there are two to six perfectly-conducting (PEC) circular-section reinforcing bars embedded in each slab sharing different size, and placed at different depth. Notice the length of the slab determines the number of A-scan measurements per B-scan. This property makes a generalized B-scan dataset that emulates the real GPR data collection condition.

Similar to [53], we use Gaussian norm wave as the pulse emitted from GPR in all our simulations, which have a central frequency  $f_c = 2.4GHz$ . The distance between transmitter and receiver of the antenna is set to  $5cm$ , while the time window is  $5ns$ . The antenna in all simulations is moving along the line orthogonal to the direction we set up the PECs. To match with the commercial GPR data collection frequency, a time sampling measurement is conducted on every consecutive trace with  $2mm$ . Note that the dielectric property of the surrounding

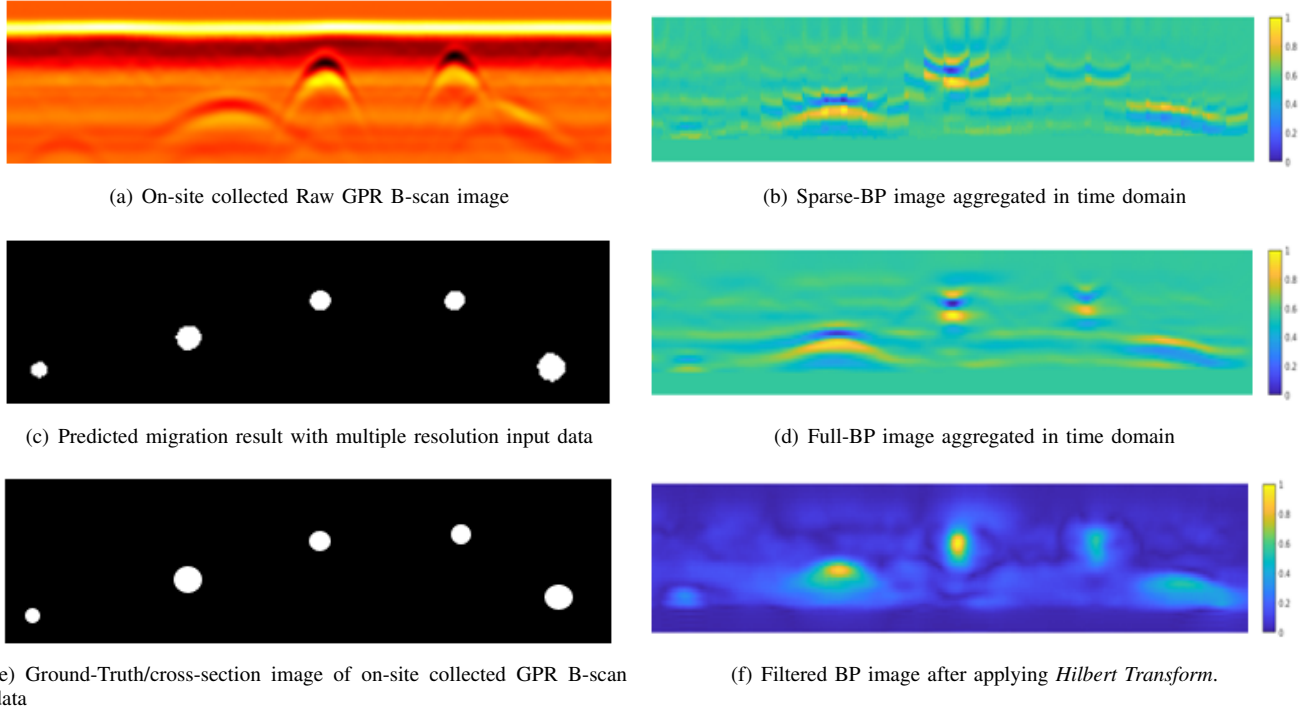


Fig. 9. Migration results comparison between our proposed migration method and conventional migration method.

medium in all our slabs is set to 7, which matches with the concrete dielectric property in the real world. The front view figure of our synthetic slabs is shown in Fig.8.

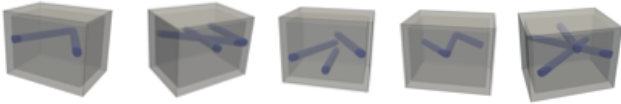


Fig. 8. Some CAD models built by gprMax, which simulate the concrete slab environment where several pipes inserted in.

We conduct 9 times synthetic GPR data collection on each simulated slab, with the same spacing between each collection. Therefore, there are 5103 B-scan data are generated in the end. We also generate the point cloud ground truth data according to the slab model we created. (The updated GPR dataset will be released once our work is accepted.)

### B. Experiments Study of MigrationNet

1) *Effectiveness of MigrationNet*: As depicted in Fig.9, Fig.9 (a) shows the collected on-site GPR B-scan data, which is illustrated in a highlighted *hotmap* format. Then, Fig.9 (b) and (d) are represented the back-projected data in the time domain, and are displayed with a highlighted *parula* color code; specifically, figure (b) shows the conventional B-scan interpretation result with a sparse input BP data, while figure (d) uses the dense BP data as input. In addition, we further apply the *Hilbert Transform* filter in figure (d). The filtered BP image is shown in figure (f) with a highlighted *parula* color code. At last, figure (e) indicates the ground truth of cross-section image for our collected on-site B-scan data, while

figure (c) demonstrates the B-scan interpretation result from *MigrationNet*.

In the meanwhile, quantitative effectiveness comparison between the conventional Migration and MigrationNet are demonstrated in Table.I. Note that in conventional migration method, the energy level is continuous distributed from 0 to 1. In contrast, the energy level in MigrationNet is binary distributed. That is, 0 stands for the background, and 1 presents the target area. Due to this reason, we convert the conventional migration results to the binary image by selecting the luminance threshold as 0.45. This luminance threshold would convert the region where energy level is greater than 0.45 to 1, and the rest of the region to 0. In this way, we can compare the GPR image reconstruction results between the conventional and learning-based methods with multiple metrics.

The metrics include *Mean IOU*, *Pixel Accuracy*, *Euclidean Distance ( $E_{distance}$ )*, *Mean Square Error (MSE)*, *Signal-to-Noise-Ratio (SNR / dB)* and *Structural Similarity Index (SSMI)*. For metrics *Mean IOU*, *Pixel Accuracy*, *SSMI*, the larger the value is, the better the performance it stands for; and vice versa for metrics *E<sub>distance</sub>*, *MSE*, *SNR*. Thus, we can conclude that MigrationNet could effectively improve the performance of GPR imaging reconstruction.

We also test noise robustness in MigrationNet. In this section, we choose to add *Gaussian white noise*, *salt & pepper noise* and *speckle noise* respectively to the GPR raw data and our stacked BP input data. We conduct 12 sets of experiments on the conventional migration method while another 12 sets of experiments on our proposed method. There are 4 different variance and noise density parameters being compared for each of the noise types. The parameter settings are 0.05, 0.1, 0.2,



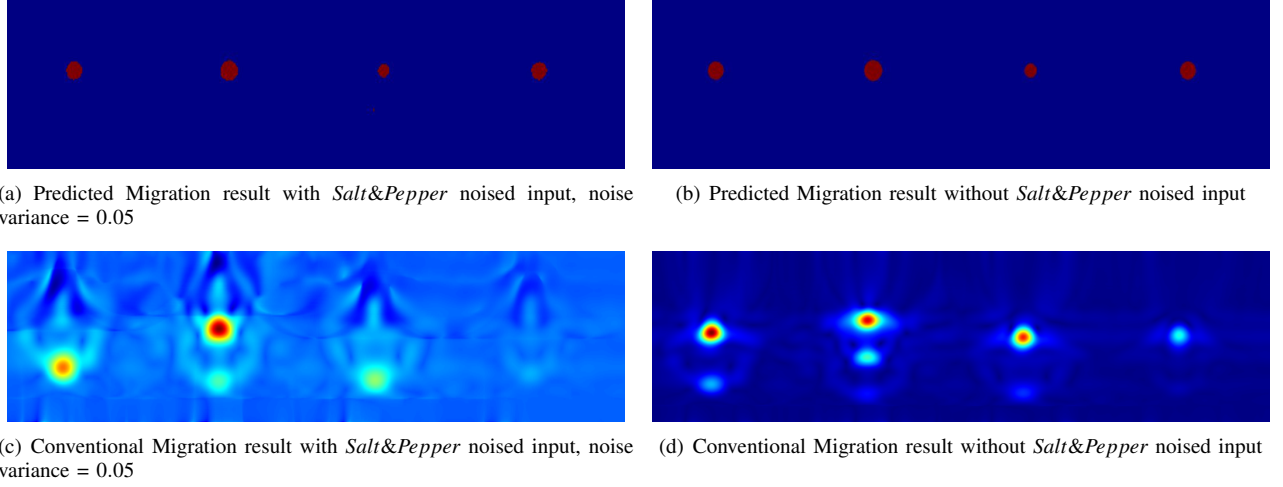


Fig. 10. Noise Robustness Comparison between conventional and proposed migration method with/without *Salt&Pepper* noised input.

TABLE I  
GPR MIGRATION EFFECTIVENESS COMPARISON BETWEEN  
CONVENTIONAL MIGRATION AND MIGRATIONNET

Metrics	Conventional Migration	MigrationNet
Mean IOU	59.15	<b>89.97</b>
Pixel Acc %	90.48	<b>95.70</b>
E_distance	1.1347e+03	<b>35.5809</b>
MSE	5.317e+03	<b>661.1313</b>
SSMI	0.7699	<b>0.9413</b>
SNR / dB	5.7474	<b>3.3066</b>

and 0.5 in each test respectively. After adding different noises to each input, we compared *root-mean-square error (RMSE)* between conventional migration method and MigrationNet.

As illustrated in Table.VII and Fig.10, we could find that our proposed method has high noise robustness, while in the conventional method, the noise would significantly influence the migration results.

2) *Ablation Study for MigrationNet: How B-scan sampling density matter?* One interesting topic is how the channel of stacked BP data, that is, the number of A-scan measurements in the spatial domain, affects the migration performance. It is known that the more A-scan data used, the better migration result (i.e., sharper, brighter, and more focused target point in the energy map) obtained. However, it is also computation costly to process such a large amount of data.

To assess our multiple spatial resolution encoder's effectiveness and investigate the best spatial resolution for input data, we conduct this experiment to verify the encoder performance with a different input resolution. Given a raw B-scan data, we extract a different number of A-scan measurements to back-project them into stack BP data format with different spatial resolution, such as the sparse input with 64 and 128 channels BP data, semi-sparse input with 128 and 256 channels BP data as well as *raw* input with all the BP data kept. Besides, we also provide single resolution input such as 64 channels input, 128 channels input, and 256 channels input. We still take *Euclidean*

*Distance (E\_distance)*, *Mean Square Error (MSE)*, *Signal-to-Noise-Ratio (SNR / dB)* and *Structural Similarity Index (SSMI)* as the metrics for evaluation. The results are summarized in Table.III.

We find that our multi-resolution-combined input gains the best performance among the comparisons. Notice when the input channel number decreases to 64, it will go beyond the MigrationNet's ability to learn spatial features from such a sparse input. We expect that the local geometrical and semantic features from back-projected data could be better extracted through the combined multi-resolution encoder. The result also indicates that our method has a better understanding of detailed information.

**How the structure similarity loss matters?** To verify the effectiveness of our joint loss, we further provide a comparison among the same metrics as demonstrated in Table.I, with/without structural similarity loss. As shown in Table.IV, our joint loss has a better performance than the single Cross-Entropy loss, which reveals that this hybrid loss design can capture both segmentation information and fine structures with clear boundaries.

### C. Experiments Study of GPRNet

1) *Effectiveness of GPRNet:* To evaluate the effectiveness of GPRNet, Fig.11 demonstrates the result of GPRNet; then, we compare with baseline methods such as PCN and TopNet [47] as shown in Fig.12. The dataset introduced in Section.V-A is used for the evaluation. Specifically, we use three evaluation metrics for the effectiveness comparison: the Chamfer Distance, Earth Mover's Distance [49] and the average  $\mathcal{L}_1$  distance. Note that  $\mathcal{L}_1$  distance is evaluated on the occupied volumetric map between the prediction and the ground truth due to the point cloud is unordered. The number of points in the predicted output is set to 12160 while the input number of points is 1500.

TABLE II  
NOISE ROBUSTNESS EVALUATION COMPARISON BETWEEN CONVENTIONAL MIGRATION AND MIGRATIONNET, ROOT-MEAN-SQUARE ERROR (RMSE) IS TAKEN AS THE EVALUATION CRITERIA IN THE FOLLOWING TESTS.

	Conventional Migration			MigrationNet		
	Gaussian	Salt & Pepper	Speckle	Gaussian	Salt & Pepper	Speckle
Without Noise	37.3491			3.3500		
Variance & Noise density = 0.05	54.3589	51.6030	56.1675	11.4624	11.2508	10.2708
Variance & Noise density = 0.1	62.2094	61.1385	61.8539	17.8093	16.3628	16.0731
Variance & Noise density = 0.2	75.3084	77.7894	76.1743	32.1583	30.9074	29.5939
Variance & Noise density = 0.5	92.4765	90.1059	92.0384	45.3853	42.8437	41.2759

TABLE III  
EVALUATION PERFORMANCE COMPARISON WITH DIFFERENT SPATIAL RESOLUTION INPUT.

Multi-Res. Input Channels	E_distance	MSE	SSMI	SNR / dB
<b>256+128+64</b>	<b>35.5809</b>	661.1313	<b>0.9413</b>	<b>3.3066</b>
256+128	43.6190	717.1609	0.9250	3.5947
128+64	51.4325	832.5777	0.9199	5.7474
256	98.2688	1.4553e+03	0.9035	7.1199
128	101.4359	1.433e+03	0.9075	7.0553
64	-	-	-	-
raw input	40.1750	<b>630.7042</b>	0.9265	3.6849

TABLE IV  
PERFORMANCE COMPARISON BETWEEN OUR JOINT LOSS AND CROSS ENTROPY LOSS

Metrics	Joint Loss	Cross Entropy Loss
Mean IOU	<b>89.97</b>	87.65
pixel Acc %	<b>95.70</b>	94.65
E_distance	<b>35.5809</b>	38.9276
MSE	<b>661.1313</b>	764.5629
SSMI	<b>0.9413</b>	0.9378
SNR / dB	<b>3.3066</b>	5.0584



Fig. 11. The representative completion results of GPRNet for 3D model reconstruction. The input 3D model is listed in Fig.8.

TABLE V  
EVALUATION PERFORMANCE COMPARISON WITH DIFFERENT BASELINES.  
CD: AVERAGE SQUARED DISTANCE BETWEEN TWO POINTS, EMD:  
AVERAGE DISTANCE BETWEEN CORRESPONDING POINTS,  $\mathcal{L}_1$ : AVERAGE  
NORM DISTANCE BETWEEN TWO VOXELS

	GPRNet	PCN	TopNet
CD	<b>6.328</b>	6.725	6.821
EMD	<b>6.536</b>	6.827	7.173
$\mathcal{L}_1$	<b>2.016</b>	2.430	2.621

Table.V indicates that our proposed method outperforms other methods in different GPR-based inspection environments. Note that all the metrics are scaled by  $10^3$  for better perception. In addition, the visualization of point cloud model is depicted in Fig.12. It lists the reconstructed point cloud

model generated by different methods. Compared to other methods. Based on the quantitative and qualitative results, our method outperforms the other methods in spatial continuity and shape accuracy level.

TABLE VI  
EVALUATION PERFORMANCE COMPARISON WITH VARIOUS LEVEL OF INCOMPLETENESS.

Incompleteness Level	CD	EMD	$\mathcal{L}_1$
1000	7.264	7.498	2.629
<b>1500</b>	6.328	6.536	2.016
2000	6.174	6.236	1.823
3000	5.524	5.563	1.585
4000	4.773	4.925	1.430

Furthermore, We analyze the effectiveness of our network with the different level of incompleteness. In Tabel.VI, we compare the performance at  $N = 1000, 1500, 2000, 3000$  and  $4000$ , where  $N$  indicates the number of input point clouds. We notice that the performance of GPRNet increases with the input incompleteness level, and the input incompleteness level in our input could still obtain a good performance.

2) *Noise Robustness of GPRNet*: To evaluate the effectiveness of our method under different sensor noise levels, we perturbed the input sparse point cloud with multiple Gaussian white noise levels, where the standard deviations are 0.01, 0.05, 0.1, and 0.2, respectively. We further making noise comparisons among GPRNet, PCN, and TopNet with different metrics: CD distance, EMD distance, and average  $\mathcal{L}_1$  distance. As illustrated in Table.VII, we could find our proposed method gains higher robustness against the noise.

3) *Field Test Model Reconstruction Comparison*: This section compares the effectiveness of the 3D reconstruction model between the proposed GPRNet and conventional migration method with the field data collected on the CCNY testbed. As illustrated in Fig.13, the black window region in Fig.13(a)

TABLE VII  
NOISE ROBUSTNESS EVALUATION ON GPRNET WITH THREE METRICS.

	GPRNet			PCN			TopNet		
	CD	EMD	$\mathcal{L}_1$ distance	CD	EMD	$\mathcal{L}_1$ distance	CD	EMD	$\mathcal{L}_1$ distance
Variance & Noise density = 0.01	6.419	6.628	2.2871	6.901	7.266	2.6187	6.894	7.024	2.5498
Variance & Noise density = 0.05	7.722	8.124	2.5648	7.965	8.313	2.7015	8.248	8.480	2.7973
Variance & Noise density = 0.1	7.774	8.068	2.6013	8.141	8.458	2.7833	8.489	8.517	2.8571
Variance & Noise density = 0.2	8.069	8.369	3.0455	8.495	8.901	2.9559	8.662	8.956	3.1304

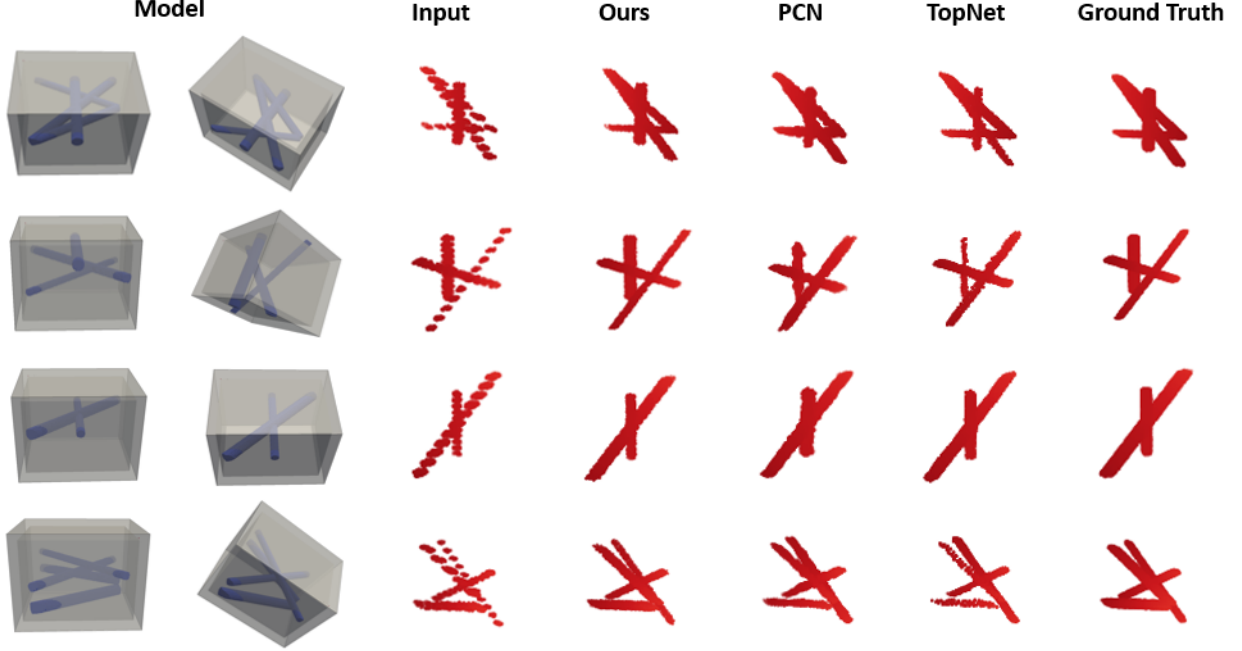


Fig. 12. The comparison of completion results between other methods and our network. From left to right: the slab CAD model, input data, PCN [6], TopNet [47], our method and the ground truth. Based on the results, our method could reconstruct a better 3D model for visualization.

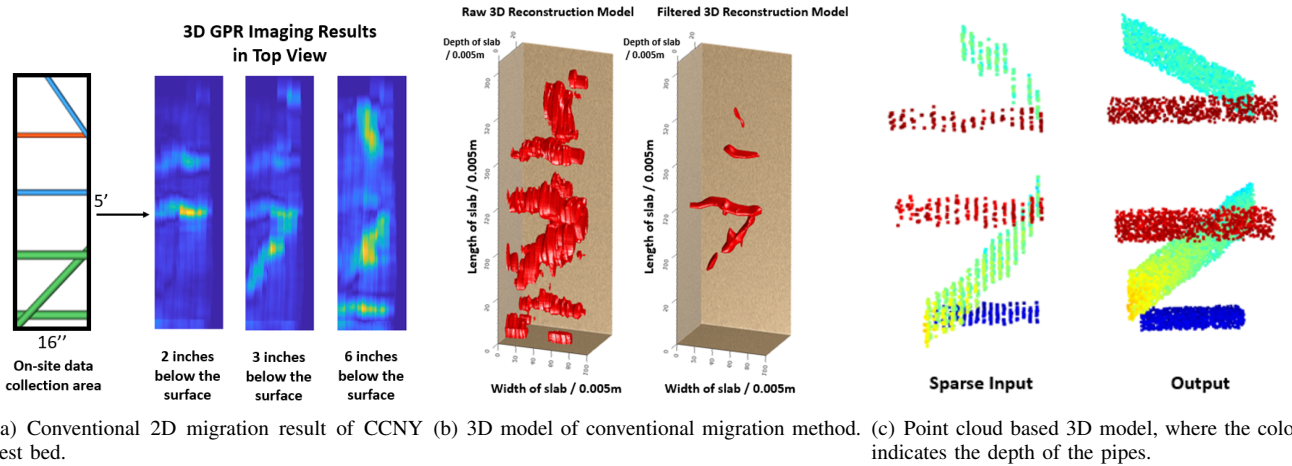


Fig. 13. An illustration of GPR 3D model results. (a) indicates the conventional migration results for our collected field data at the CCNY test bed/concrete slab. (b) shows both the raw and filtered 3D model from the migration result, while (c) shows our proposed 3D reconstruction method, which could reconstruct the 3D point cloud model from the sparse input.

indicates the data collection area while the three 2D images demonstrates migration results from the top view. Note that the red pipe in Fig.13(a) could not be recovered, the reason is that its depth is out of the GPR detection range (See Fig.7

for concrete slab details). Furthermore, we also illustrate raw and filtered 3D model generated by conventional migration methods in Fig.13(b). Due to the limitation of the conventional migration method, the noise data is hard to be cleaned out

and differentiated from the raw GPR data, which causes the filtered 3D model is still hard to be recognized by normal GPR users. At last, Fig.13(c) illustrates the proposed 3D model reconstruction method, where the color represents the depth of the pipe. Note that in field test, the positioning accuracy would affect the distribution of the sparse input, which would introduce the noise in reconstituted point cloud model. However, under the supervision of the ground truth, the model could cover the uneven distributed area and fill up with point clouds, to reveal the real 3D model of the target. As we can see, compared with the traditional migration method, our method only requires a sparse input and further generate a fine and continuous output 3D model of underground pipes. It facilitates the GPR users to understand the complex raw GPR B-scan data. In addition to the better performance, using the proposed GPR-based robotic inspection platform, the data-collection time is also extremely reduced. Without the robotic data collection platform, the inspector has to push the GPR device along straight lines and move the GPR antenna from one spot to another, which would take around 5 minutes to scan a 16" by 5' area. However, our robotic-based data collection only needs less than one minute to automated scan the same area, which provides a more efficient way for GPR survey.

## VI. CONCLUSION

This paper presents a novel GPR-based 3D model reconstruction system for underground utilities by using an omni-directional robot. Our omni-directional robot allows the GPR device to move forward, backward, and sideways without rotations. The proposed system can reconstruct the underground utility model represented as a 3D point cloud map. According to the experiments, our approach could obtain a fine 3D model for a better visualization while finding out our method has higher robustness against noise.

## ACKNOWLEDGMENT

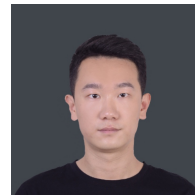
Financial support for this study was provided by NSF grant IIP-1915721, and by the U.S. Department of Transportation, Office of the Assistant Secretary for Research and Technology (USDOT/OST-R) under Grant No. 69A3551747126 through INSPIRE University Transportation Center (<http://inspire-utc.mst.edu>) at Missouri University of Science and Technology. The views, opinions, findings and conclusions reflected in this publication are solely those of the authors and do not represent the official policy or position of the USDOT/OST-R, or any State or other entity. J Xiao has significant financial interest in InnovBot LLC, a company involved in R&D and commercialization of the technology.

## REFERENCES

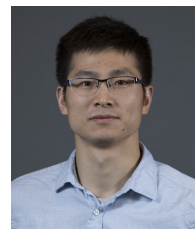
- [1] S. Demirci, E. Yigit, I. H. Eskidemir, and C. Ozdemir, "Ground penetrating radar imaging of water leaks from buried pipes based on back-projection method," *Ndt & E International*, vol. 47, pp. 35–42, 2012.
- [2] GPR-SURVEY, "Gpr-slice," [https://users.neo.registeredsite.com/4/6/6/22358664/assets/GPR-SLICE\\_Software\\_Manual\\_2021.pdf/](https://users.neo.registeredsite.com/4/6/6/22358664/assets/GPR-SLICE_Software_Manual_2021.pdf/), 2021.
- [3] leica geosystems, "Leica ds2000 gpr," <https://leica-geosystems.com/en-us/products/detection-systems/utility-detection-solutions/leica-ds2000-utility-detection-radar/>, 2021.
- [4] usradar, "Quantum mini dual-frequency concrete scanner," <https://usradar.com/quantum-mini-concrete-scanner/>, 2021.
- [5] J. Feng, L. Yang, H. Wang, Y. Song, and J. Xiao, "Gpr-based subsurface object detection and reconstruction using random motion and depthnet," in *2020 IEEE International Conference on Robotics and Automation (ICRA)*. IEEE, 2020, pp. 7035–7041.
- [6] W. Yuan, T. Khot, D. Held, C. Mertz, and M. Hebert, "Pcn: Point completion network," in *2018 International Conference on 3D Vision (3DV)*. IEEE, 2018, pp. 728–737.
- [7] W. A. Schneider, "Integral formulation for migration in two and three dimensions," *Geophysics*, vol. 43, no. 1, pp. 49–76, 1978.
- [8] X. Liu, M. Serhir, A. Kameni, M. Lambert, and L. Pichon, "Ground penetrating radar data imaging via kirchhoff migration method," in *2017 International Applied Computational Electromagnetics Society Symposium-Italy (ACES)*. IEEE, 2017, pp. 1–2.
- [9] N. Smitha, D. U. Bharadwaj, S. Abilash, S. Sridhara, and V. Singh, "Kirchhoff and fk migration to focus ground penetrating radar images," *International Journal of Geo-Engineering*, vol. 7, no. 1, p. 4, 2016.
- [10] J. Gazdag, "Wave equation migration with the phase-shift method," *Geophysics*, vol. 43, no. 7, pp. 1342–1351, 1978.
- [11] I. Lecomte, S.-E. Hamran, and L.-J. Gelius, "Improving kirchhoff migration with repeated local plane-wave imaging? a sar-inspired signal-processing approach in prestack depth imaging," *Geophysical Prospecting*, vol. 53, no. 6, pp. 767–785, 2005.
- [12] J. F. Claerbout and S. M. Doherty, "Downward continuation of moveout-corrected seismograms," *Geophysics*, vol. 37, no. 5, pp. 741–768, 1972.
- [13] S. Demirci, H. Cetinkaya, E. Yigit, C. Ozdemir, and A. A. Vertiy, "A study on millimeter-wave imaging of concealed objects: Application using back-projection algorithm," *Progress In Electromagnetics Research*, vol. 128, pp. 457–477, 2012.
- [14] R. Schofield, L. King, U. Tayal, I. Castellano, J. Stirrup, F. Pontana, J. Earls, and E. Nicol, "Image reconstruction: Part 1—understanding filtered back projection, noise and image acquisition," *Journal of cardiovascular computed tomography*, vol. 14, no. 3, pp. 219–225, 2020.
- [15] M. A. González-Huici, I. Catapano, and F. Soldovieri, "A comparative study of gpr reconstruction approaches for landmine detection," *IEEE Journal of Selected Topics in Applied Earth Observations and Remote Sensing*, vol. 7, no. 12, pp. 4869–4878, 2014.
- [16] X. Xie, J. Zhai, and B. Zhou, "Back-fill grouting quality evaluation of the shield tunnel using ground penetrating radar with bi-frequency back projection method," *Automation in Construction*, vol. 121, p. 103435, 2020.
- [17] L. Zhou, C. Huang, and Y. Su, "A fast back-projection algorithm based on cross correlation for gpr imaging," *IEEE Geoscience and Remote Sensing Letters*, vol. 9, no. 2, pp. 228–232, 2011.
- [18] A. Gharamohammadi, F. Behnia, and A. Shokouhmand, "Imaging based on a fast back-projection algorithm considering antenna beamwidth," in *2019 Sixth Iranian Conference on Radar and Surveillance Systems*. IEEE, 2019, pp. 1–4.
- [19] J. Cai, P. Peng, H. Zeng, and S. Wang, "A cross correlation based back-projection imaging method for through-wall imaging," in *Journal of Physics: Conference Series*, vol. 1607, no. 1. IOP Publishing, 2020, p. 012020.
- [20] C. Lin, X. Wang, Y. Li, F. Zhang, Z. Xu, and Y. Du, "Forward modelling and gpr imaging in leakage detection and grouting evaluation in tunnel lining," *KSCE Journal of Civil Engineering*, vol. 24, no. 1, pp. 278–294, 2020.
- [21] S. Jacobsen and Y. Birkelund, "Improved resolution and reduced clutter in ultra-wideband microwave imaging using cross-correlated back projection: Experimental and numerical results," *Journal of Biomedical Imaging*, vol. 2010, p. 20, 2010.
- [22] H. Zhang, O. Shan, G. Wang, J. Li, S. Wu, and F. Zhang, "Back-projection algorithm based on self-correlation for ground-penetrating radar imaging," *Journal of Applied Remote Sensing*, vol. 9, no. 1, p. 095059, 2015.
- [23] H. Liu, Z. Chen, H. Lu, F. Han, C. Liu, J. Li, and J. Cui, "Migration of ground penetrating radar with antenna radiation pattern correction," *IEEE Geoscience and Remote Sensing Letters*, 2020.
- [24] N. Chetih and Z. Messali, "Tomographic image reconstruction using filtered back projection (fbp) and algebraic reconstruction technique (art)," in *2015 3rd International Conference on Control, Engineering & Information Technology (CEIT)*. IEEE, 2015, pp. 1–6.
- [25] H. Li, C. Chou, L. Fan, B. Li, D. Wang, and D. Song, "Toward automatic subsurface pipeline mapping by fusing a ground-penetrating radar and



- a camera,” *IEEE Transactions on Automation Science and Engineering*, vol. 17, no. 2, pp. 722–734, 2019.
- [26] C. Chou, S.-H. Yeh, J. Yi, and D. Song, “Extrinsic calibration of a ground penetrating radar,” in *2016 IEEE International Conference on Automation Science and Engineering (CASE)*. IEEE, 2016, pp. 1326–1331.
- [27] C. Chou, S.-H. Yeh, and D. Song, “Mirror-assisted calibration of a multi-modal sensing array with a ground penetrating radar and a camera,” in *2017 IEEE/RSJ International Conference on Intelligent Robots and Systems (IROS)*. IEEE, 2017, pp. 1457–1463.
- [28] C. Chou, A. Kingery, D. Wang, H. Li, and D. Song, “Encoder-camera-ground penetrating radar tri-sensor mapping for surface and subsurface transportation infrastructure inspection,” in *2018 IEEE International Conference on Robotics and Automation (ICRA)*. IEEE, 2018, pp. 1452–1457.
- [29] H. Li, C. Chou, L. Fan, B. Li, D. Wang, and D. Song, “Robotic subsurface pipeline mapping with a ground-penetrating radar and a camera,” in *2018 IEEE/RSJ International Conference on Intelligent Robots and Systems (IROS)*. IEEE, 2018, pp. 3145–3150.
- [30] C. Chou, H. Li, and D. Song, “Encoder-camera-ground penetrating radar sensor fusion: Bimodal calibration and subsurface mapping,” *IEEE Transactions on Robotics*, 2020.
- [31] M. Pereira, Y. Zhang, D. Orfeo, D. Burns, D. Huston, and T. Xia, “3d tomography for multistatic gpr subsurface sensing,” in *Radar Sensor Technology XXII*, vol. 10633. International Society for Optics and Photonics, 2018, p. 1063302.
- [32] M. Pereira, Y. Zhang, D. Huston, and T. Xia, “3-d sar imaging for multistatic gpr,” in *Image Sensing Technologies: Materials, Devices, Systems, and Applications VI*, vol. 10980. International Society for Optics and Photonics, 2019, p. 109801D.
- [33] M. Pereira, Y. Zhang, D. Orfeo, D. Burns, D. Huston, and T. Xia, “3d tomographic image reconstruction for multistatic ground penetrating radar,” in *2019 IEEE Radar Conference (RadarConf)*. IEEE, 2019, pp. 1–6.
- [34] M. Pereira, D. Burns, D. Orfeo, Y. Zhang, L. Jiao, D. Huston, and T. Xia, “3-d multistatic ground penetrating radar imaging for augmented reality visualization,” *IEEE Transactions on Geoscience and Remote Sensing*, 2020.
- [35] M. Pereira, D. Burns, D. Orfeo, R. Farrel, D. Hutson, and T. Xia, “New gpr system integration with augmented reality based positioning,” in *Proceedings of the 2018 on Great Lakes Symposium on VLSI*, 2018, pp. 341–346.
- [36] L. Yang, G. Yang, Z. Liu, Y. Chang, B. Jiang, Y. Awad, and J. Xiao, “Wall-climbing robot for visual and gpr inspection,” in *2018 13th IEEE Conference on Industrial Electronics and Applications (ICIEA)*. IEEE, 2018, pp. 1004–1009.
- [37] H. Liu, C. Lin, J. Cui, L. Fan, X. Xie, and B. F. Spencer, “Detection and localization of rebar in concrete by deep learning using ground penetrating radar,” *Automation in Construction*, vol. 118, p. 103279, 2020.
- [38] J. Gao, D. Yuan, Z. Tong, J. Yang, and D. Yu, “Autonomous pavement distress detection using ground penetrating radar and region-based deep learning,” *Measurement*, p. 108077, 2020.
- [39] S. Khudoyarov, N. Kim, and J.-J. Lee, “Three-dimensional convolutional neural network-based underground object classification using three-dimensional ground penetrating radar data,” *Structural Health Monitoring*, p. 1475921720902700, 2020.
- [40] U. Ozkaya, F. Melgani, M. B. Bejiga, L. Seyfi, and M. Donelli, “Gpr b scan image analysis with deep learning methods,” *Measurement*, p. 107770, 2020.
- [41] T.-Y. Lin, P. Dollár, R. Girshick, K. He, B. Hariharan, and S. Belongie, “Feature pyramid networks for object detection,” in *Proceedings of the IEEE conference on computer vision and pattern recognition*, 2017, pp. 2117–2125.
- [42] O. Ronneberger, P. Fischer, and T. Brox, “U-net: Convolutional networks for biomedical image segmentation,” in *International Conference on Medical image computing and computer-assisted intervention*. Springer, 2015, pp. 234–241.
- [43] Z. Zhou, M. M. R. Siddiquee, N. Tajbakhsh, and J. Liang, “Unet++: A nested u-net architecture for medical image segmentation,” in *Deep Learning in Medical Image Analysis and Multimodal Learning for Clinical Decision Support*. Springer, 2018, pp. 3–11.
- [44] Z. Wang, A. C. Bovik, H. R. Sheikh, and E. P. Simoncelli, “Image quality assessment: from error visibility to structural similarity,” *IEEE transactions on image processing*, vol. 13, no. 4, pp. 600–612, 2004.
- [45] H. Zhao, O. Gallo, I. Frosio, and J. Kautz, “Loss functions for neural networks for image processing,” *arXiv preprint arXiv:1511.08861*, 2015.
- [46] C. Godard, O. Mac Aodha, and G. J. Brostow, “Unsupervised monocular depth estimation with left-right consistency,” in *Proceedings of the IEEE Conference on Computer Vision and Pattern Recognition*, 2017, pp. 270–279.
- [47] L. P. Tchapmi, V. Kosaraju, H. Rezaatofghi, I. Reid, and S. Savarese, “Topnet: Structural point cloud decoder,” in *Proceedings of the IEEE Conference on Computer Vision and Pattern Recognition*, 2019, pp. 383–392.
- [48] C. R. Qi, H. Su, K. Mo, and L. J. Guibas, “Pointnet: Deep learning on point sets for 3d classification and segmentation,” in *Proceedings of the IEEE conference on computer vision and pattern recognition*, 2017, pp. 652–660.
- [49] P. Achlioptas, O. Diamanti, I. Mitliagkas, and L. Guibas, “Learning representations and generative models for 3d point clouds,” in *International conference on machine learning*. PMLR, 2018, pp. 40–49.
- [50] Y. Yang, C. Feng, Y. Shen, and D. Tian, “Foldingnet: Point cloud auto-encoder via deep grid deformation,” in *Proceedings of the IEEE Conference on Computer Vision and Pattern Recognition*, 2018, pp. 206–215.
- [51] Z. Huang, Y. Yu, J. Xu, F. Ni, and X. Le, “Pf-net: Point fractal network for 3d point cloud completion,” in *Proceedings of the IEEE/CVF Conference on Computer Vision and Pattern Recognition*, 2020, pp. 7662–7670.
- [52] C. Warren, A. Giannopoulos, and I. Giannakis, “gprmax: Open source software to simulate electromagnetic wave propagation for ground penetrating radar,” *Computer Physics Communications*, vol. 209, pp. 163–170, 2016.
- [53] S. Meschino and L. Pajewski, “Spot-gpr: A freeware tool for target detection and localization in gpr data developed within the cost action tu1208,” *Journal of Telecommunications and Information Technology*, 2017.

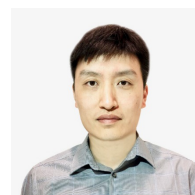


**Jinglun Feng** was born in Jinan, Shandong, China. He received his Master degree in control engineering from the Shandong University in 2015. He is currently pursuing the Ph.D. degree in electrical engineering with City College of New York, CUNY, New York, NY, USA. His research interests computer vision, structural health monitoring, visual SLAM and reconstruction, multi-sensor fusion, and robotic control.



visual SLAM and reconstruction, multi-sensor fusion, and robotic control.

**Liang Yang** received his B.S. degree from Shenyang Aerospace University, Shenyang, China in 2012, and PhD degree in electronics engineering from the City College of New York (CUNY City College) in 2019, and PhD degree in pattern recognition and intelligent system from University of Chinese Academy of Sciences in 2019. He joined APPLE as a senior 3D computer vision researcher in 2019, and currently working on 3D visual perception and understanding. His research interests cover motion and path planning, 3D perception and understanding, visual SLAM and reconstruction, multi-sensor fusion, and robotic control.



**Biao Jiang** was born in Jiangsu, China. He received a Master in Interdisciplinary Studies in 2010, and a PhD in Electrical Engineering in 2013 from the City College of the City University of New York (CUNY), USA. He currently works at the Robotics Lab of City College of New York as a research scientist. His research interests include computer vision, SLAM and wireless communication.



**Jizhong Xiao** is a Professor of Electrical Engineering at the City College of New York (CCNY/CUNY City College) and a doctoral faculty member of the Ph.D. program in Computer Science at CUNY Graduate Center. He received his Ph.D. degree from Michigan State University in 2002, M.E. degree from Nanyang Technological University, Singapore in 1999, M.S. and B.S. degrees from the East China Institute of Technology, Nanjing, China, in 1993 and 1990, respectively. He started the robotics research program at CCNY in 2002 as the founding director of CCNY Robotics Lab. His current research interests include robotics and control, cyberphysical systems, autonomous navigation and 3D simultaneous localization and mapping (SLAM), real-time and embedded computing, assistive technology, multiagent systems and swarm robotics. He has published more than 160 research articles in peer reviewed journal and conferences. He received the U.S. National Science Foundation CAREER Award in 2007, the CCNY Outstanding Mentor Award in 2011, and the Humboldt Research Fellowship for Experienced Researchers from the Alexander von Humboldt Foundation, Germany, from 2013 to 2015. He is a senior member of IEEE.